Article

Analysis of the Mechanical Properties of the Reconstituted Hydrate-Bearing Clayey-Silt Samples from the South China Sea

Lin Dong [1,2], Hualin Liao [2,3], Yanlong Li [1,4,*], Qingguo Meng [1,4], Gaowei Hu [1,4], Jintang Wang [2,3] and Nengyou Wu [1,4,*]

1   The Key Laboratory of Gas Hydrate, Ministry of Natural Resources, Qingdao Institute of Marine Geology, Qingdao 266071, China; ddzhang@qnlm.ac (L.D.); mqingguo@mail.cgs.gov.cn (Q.M.); gwhu@qnlm.ac (G.H.)
2   Laboratory of Unconventional Oil & Gas Development, China University of Petroleum (East China), Ministry of Education, Qingdao 266580, China; liaohualin@upc.edu.cn (H.L.); wangjintang@upc.edu.cn (J.W.)
3   College of Petroleum Engineering, China University of Petroleum, Qingdao 266555, China
4   Laboratory for Marine Mineral Resources, Qingdao National Laboratory for Marine Science and Technology, Qingdao 266237, China
*   Correspondence: ylli@qnlm.ac (Y.L.); wuny@ms.giec.ac.cn (N.W.)

Abstract: Mechanical properties of hydrate-bearing sediments (HBS) are crucial for evaluating drilling- and production-induced geo-hazards. However, investigations on mechanical behaviors of clayey-silt samples containing hydrate are insufficient due to low efficiency in preparing reconstituted hydrate-bearing samples. Herein, we carried out a series of triaxial shear tests to analyze the deformation behaviors of reconstituted clayey-silt samples containing tetrahydrofuran (THF) hydrate. The sediments were taken from the Shenhu Area, northern South China Sea. The failure mechanisms during shearing are discussed based on micro-to-macro analyses. The results imply that the stress-strain curves show obvious strain-hardening under triaxial shearing, which can be divided into elastic deformation stage, transitional stage, and plastic deformation stage. Besides, the results reveal that cohesion strengthens from 0.09 MPa to 1.28 MPa when hydrate saturation increases from 15% to 60%. Moreover, calculation models are proposed to evaluate failure strengths and Young's modulus. Establishing empirical formula based on experimental data can quickly determine the strength parameters with knowing the hydrate saturation and stress state of clayey-silt sediments containing hydrate. It is urgent in field operations and numerical simulation to use reliable empirical models.

Keywords: natural gas hydrate; mechanical properties; triaxial shearing tests; clayey silt; failure mechanisms; failure strength

1. Introduction

Natural gas hydrate (NGH) has become one of the most promising clean energies with the characteristics of huge reserves, widespread distribution, and less pollution [1–3]. The hydrate-bearing sediments (HBS) are natural soils containing gas, water, and hydrate [4], which have strong relations with geological hazards such as submarine landslides [5], production [6,7], and wellbore stability [8,9]. Consequently, it is indispensable to predict mechanical responses of HBS during the NGH development.

Synthesized and pressure-core samples containing hydrate have been investigated through the method of combining theoretical analyses and laboratory experiments [10,11]. Triaxial shear tests of HBS reveal influential factors and their controlling mechanisms on mechanical behaviors. Influential factors include but are not limited to hydrate saturation, effective confining pressure, fines contents, temperature, and micro-modes of hydrate distribution [12–16]. Both the strength and stiffness are proved to be enhanced obviously with hydrate saturation [17]. Characteristics of strain-softening and strain-hardening transform change with hydrate saturation and confining pressure [18].

Compared with sand sediments, laboratory tests on silt sediments containing hydrate show differences in mechanical behaviors [19–21], which indicate that the strength and stiffness are influenced not only by hydrate saturation but by the particle size and clay content [22,23]. Furthermore, experiments conducted on pressure cores found that mechanical properties of reconstituted samples containing hydrate are similar to that of pressure cores [24,25]. Thus, the investigation of reconstituted samples can deepen understanding of the mechanical behaviors of gas hydrate reservoirs [17,26]. Besides, Luo et al. [27,28] investigated the mechanical characteristics of artificial kaolin samples and remolded marine sediments. The results indicate that the hydrate-bearing clay can be used as a substitute for marine sediments from hydrate reservoirs. Meanwhile, the samples formed with gas hydrate are limited in lower saturation [27]. However, it should be noted that present investigations on silt sediments containing hydrate are limited to lower saturation or artificial samples, which cannot characterize the strength and stiffness of reservoirs [29]. Therefore, it is more accurate and reliable in evaluating the strength parameters of HBS by using reconstituted samples from the actual natural gas hydrate reservoirs.

This study presents a series of triaxial shear tests to analyze mechanical characteristics and failure mechanisms of sediments from the Shenhu area. The THF solution is used as a substitute to form hydrate. Failure mechanism is investigated at the micro-level to explain the characteristics of strain hardening. The failure strength will be analyzed and predicted based on the improved Drucker-Prager criterion. Furthermore, Young's modulus E_{50} is estimated by analyzing experimental results and using empirical models. This work can provide a reference for the mechanical parameter estimation and risk management during natural gas hydrate development in the South China Sea.

2. Materials and Methods

2.1. Experimental Apparatus

Figure 1 illustrates the triaxial shear test apparatus. A detailed introduction of the experimental apparatus can be found in our previous publications [14,20,30,31]. The device is mainly composed of a hydrate synthesis unit, a loading unit, a pressure and temperature control unit, a fluid delivery unit, and a data acquisition unit. A cylindrical specimen can be prepared through the in-situ synthesis method in the pressure chamber [21,32,33]. The specimen is 39.1 mm in diameter and 120 mm in height. The confining pressure can be adjusted from 0 MPa to 15 MPa. The temperature can be controlled from −20 °C to 40 °C with an accuracy of ±0.1 °C. The axial load capacity is 50 kN.
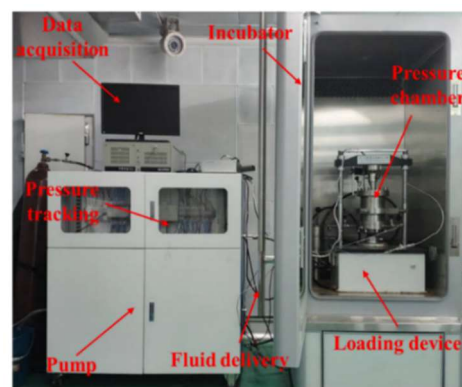
Figure 1. Schematic diagram of the triaxial test apparatus.

2.2. Materials

THF with a purity of 99.9% and marine sediment are used to prepare the reconstituted samples in this study. The host marine sediment is from the natural gas hydrate reservoir in the Shenhu area of the northern South China Sea. Its chemical composition is close to silty clay [34,35]. Its grain size distribution is shown in Figure 2. It can be observed that the

sediments are mostly composed of silt and clay. The fractions of the fine sand (63–250 μm), silt (4–63 μm), and clay (<4 μm) account for ~1%, ~63%, and ~36%, respectively [36,37]. The fractions of fine grains (less than 63μm) in the sediments are more than 99%. The porosity is about 43% and the density is 1.77 g/cm^3. The initial water content of sediments from the South China Sea is 16.48% [18].
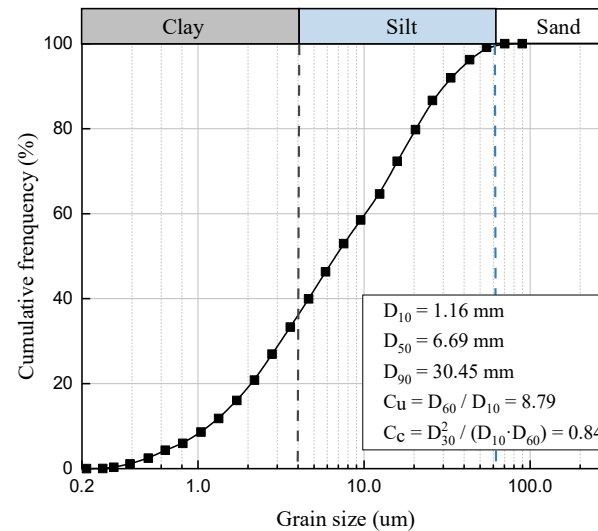

Figure 2. Grain size distribution (modified on [36,37]).

2.3. Experimental Procedures

To evaluate the mechanical characteristics of HBS and analyze the interactions between the THF hydrate and sediment particles, a series of triaxial shear tests were designed with hydrate saturation of 15%, 30%, 45%, and 60%, at the effective confining pressures of 1 MPa, 2 MPa, and 4 MPa, respectively.

Dry marine sediment (~210 g) is mixed with a certain amount of THF solution and pressed into the flexible bucket. The amount of solution can be predetermined according to desired hydrate saturation and the mass ratio [21]. Next, the reactor is placed into an inductor after connecting sensors and pipelines. Afterward, the temperature is set at 1 °C, under which the THF would be transformed into hydrate. Finally, the dry nitrogen gas is injected into the pressure chamber and the pore pressure gradually increases to the desired value (i.e., 4.5 MPa), while the confining pressure is kept at 5.5 MPa, 6.5 MPa, and 8.5 MPa, respectively. Namely, the effective confining pressure is kept at 1 MPa, 2 MPa, and 4 MPa throughout the tests. The samples are sheared at a constant strain rate of 0.75 %/min. The data of loading force and deformation are acquired during tests.

3. Results and Discussion

3.1. Failure Strength

The basic stress-strain curves have been described in our previous study [30], which is shown in Figure 3. It can be seen from Figure 3 that all stress-strain curves show the strain-hardening failure mode, and the curves can be divided into three parts, namely elastic deformation stage (I), transitional stage (II), and plastic deformation stage (III). In the elastic deformation stage, the deviator stress increases rapidly with axial strain increasing and the correlation is approximately linear. However, in the plastic deformation stage, it increases slowly as the axial strain reaches 3%. This paper would mainly emphasize the failure strength, Young's modulus, cohesion, and internal friction angle.
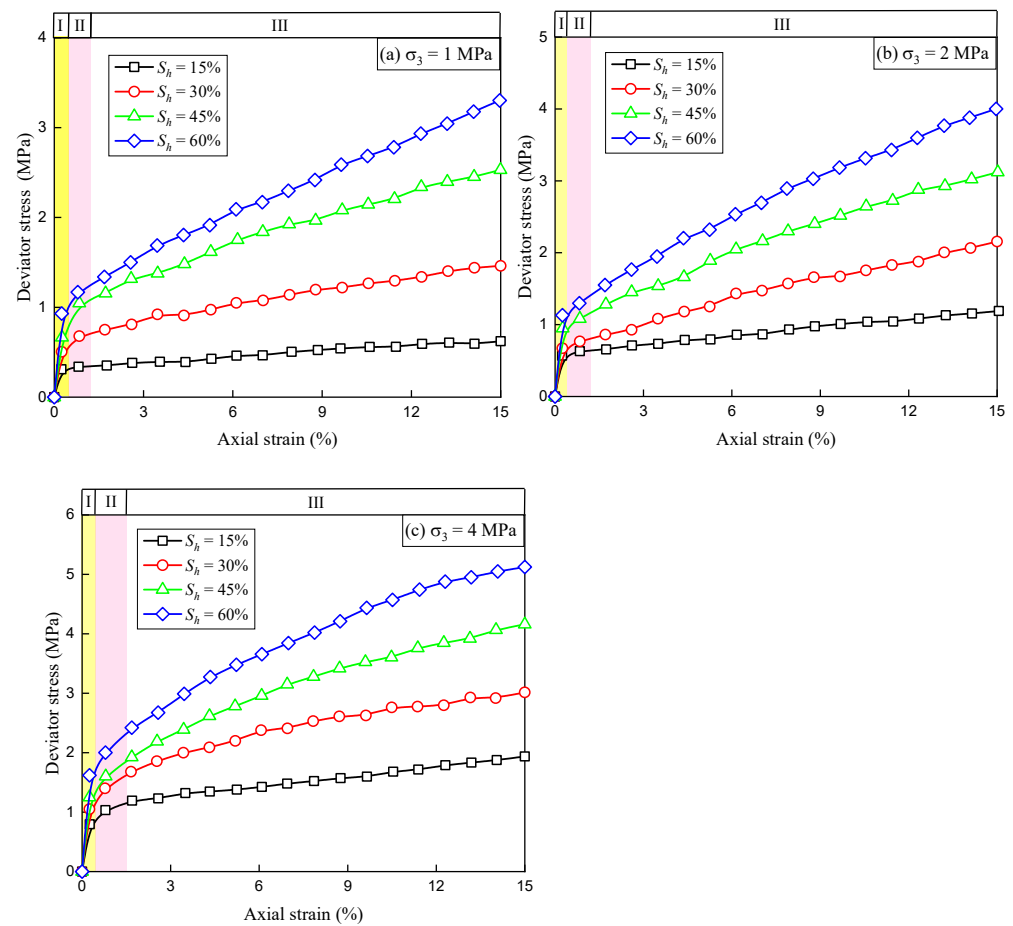
Figure 3. Stress-strain relationship of samples under various conditions (based on [30]): (**a**) σ_3 = 1 MPa; (**b**) σ_3 = 2 MPa; (**c**) σ_3 = 4 MPa.

Additionally, the mechanical properties of reconstituted clayey-silt samples are different from that of sand. The stress-strain curves of clayey silt show the strain hardening characteristics during the shearing process, while that of sand shows both strain hardening and strain softening characteristics. Besides, the failure strength is lower than that of sand under the same test conditions.

Generally, failure strength is considered as the maximum deviator stress of the samples at a specific confining pressure before the axial strain exceeds 15% [38]. Figure 4 demonstrates the relationships between failure strength and hydrate saturation [21–23,27]. The results indicate that failure strength almost increases linearly with hydrate saturation in samples. That verifies the impact of hydrate cementation on the strength and stiffness of sediments [39]. Besides, failure strength with the same hydrate saturation increases with the effective confining pressure rising.

3.2. Young's Modulus E_{50}

The Young's modulus E_{50} is defined as Young's modulus at 50% of the maximum deviator stress. Figure 5 displays the relationships between Young's modulus E_{50} and hydrate saturation. Young's modulus increases remarkably with the increase in the hydrate saturation, which is affected by effective confining pressure. Meanwhile, the value of Young's modulus varies from 19.4–141.1 MPa, indicating that the value is in a reasonable range compared with the previous studies [21–23,27].
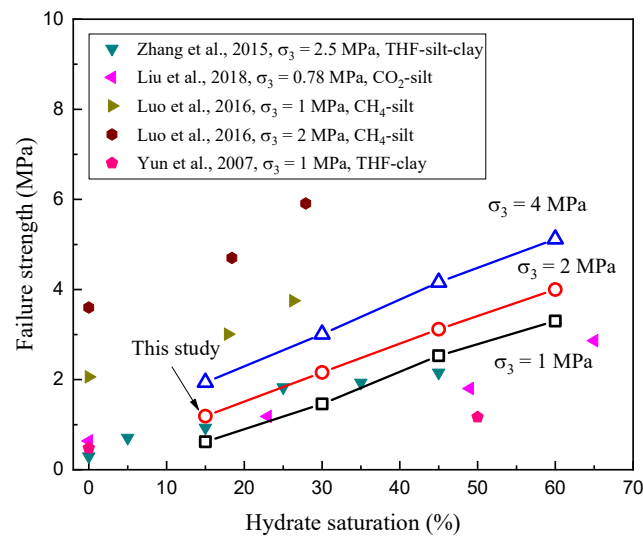
Figure 4. The failure strength of specimen versus hydrate saturation (based on [21–23,27]).
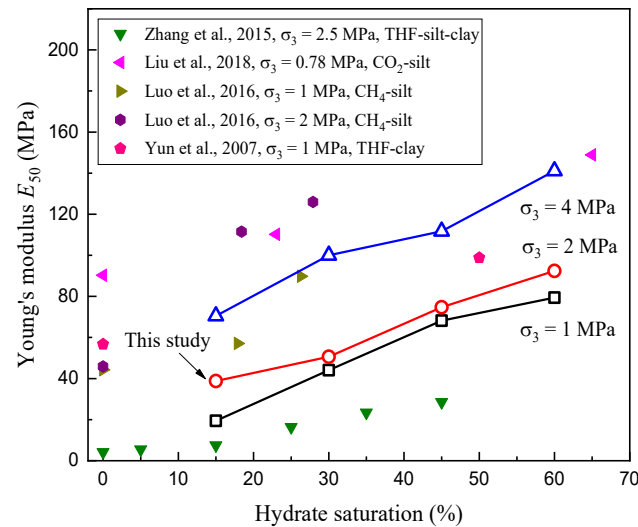

Figure 5. Variation of Young's modulus E_{50} with hydrate saturation (based on [21–23,27]).

In addition, both strength and Young's modulus of clayey-silt samples are different from that of sandy sediments containing hydrate, which reflects the effect of sediment characteristics and hydrate types on reconstituted clayey-silt samples in this paper. The samples from the Shenhu area are different from the sandy sediments in sediment types, particle size distribution, hydrate types, cementation among particles, and so on.

3.3. Cohesion and Internal Friction Angle

Figure 6 exhibits the variation of cohesion of the sediments containing THF hydrate. The results show that the cohesion of HBS increases from 0.09 MPa to 1.28 MPa when hydrate saturation increases from 15% to 60%. The filling of pores with hydrate crystal and the cementation among sediment particles enhance the strength of HBS with hydrate formation, resulting in a significant increase in cohesion. The cohesion increasing tendency is similar to those observed in previous research results [21–23,26], which verifies the accuracy of these tests.
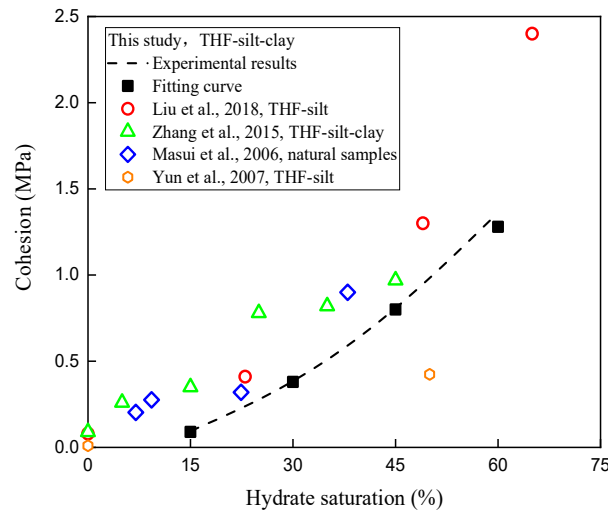
Figure 6. The relationship between the cohesion and hydrate saturation (based on [21–23,26]).

The relationship between the internal friction angles and hydrate saturation is depicted in Figure 7. The variation range of internal friction angle is 8.3–12.3°. Compared with the previous studies, the tendency of increasing the internal friction angle is different from other results, but the value of the internal friction angle in this work is reasonable [21–23,26]. Additionally, the silty-clay samples containing THF hydrate have a low value in internal friction angle compared to hydrate-bearing sand, which illustrates that sediment types have a marked effect on strength parameters [17].
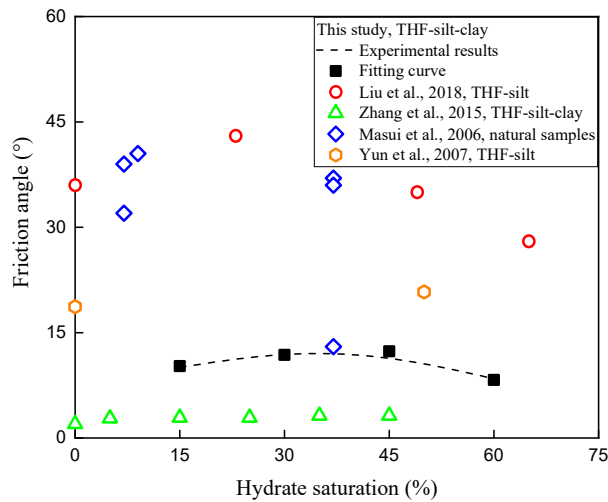
Figure 7. The relationship between the internal friction angle and hydrate saturation (based on [21–23,26]).

As shown in Figures 6 and 7, cohesion can be expressed as an exponential function of hydrate saturation. Internal friction angle and hydrate saturation are related to the quadratic function. The cohesion and internal friction angle can be calculated through Equations (1) and (2).

$$c = 0.00051 S_h^{1.93} \tag{1}$$

$$\varphi = -0.0063 \cdot S_h^2 + 0.44 \cdot S_h + 4.9 \tag{2}$$

where c and φ are cohesion (MPa) and internal friction angle (°), respectively; S_h represents the hydrate saturation, (%).

3.4. Failure Mechanisms during the Shear Process

The occurrence of hydrate leads to changes in microstructure and mechanical behaviors of HBS. Combining the controlling mechanisms and laboratory tests, the pore-scale mechanism of reconstituted hydrate-bearing clayey-silt samples from the Shenhu area is discussed to describe deformation characteristics and the impact of hydrate formation on strength parameters.

Figure 8 illustrates the SEM images of clayey-silt sediment (a–d) and sand sediment (e,f). The results show that different particles of clayey-silt sediment have characteristics of different shapes with rough and uneven surfaces, while the surface of the sand is relatively smooth. Besides, the existence of clay particles modifies the structure of host sediment and structure strength directly [17,22], which is mainly caused by the size, morphology, and cementation of clay. Therefore, the particles of clayey-silt sediment aggregate into clusters with adhesion force among particles.
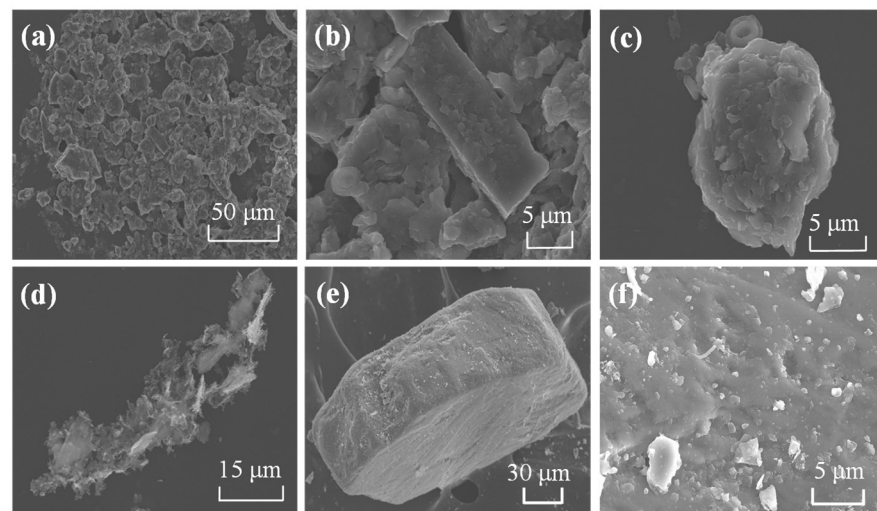

Figure 8. SEM images of sediments: (**a–d**) Clayey-silt sediment; (**e,f**) sand sediment.

At low hydrate saturation, the effect of hydrate on strength parameters is limited because of the low cementation among sediment particles induced by hydrate formation. Relative movement among sediment particles will occur easily under the combined axial and lateral loads [22,38]. Correspondingly, damage and breakage of hydrate may occur along with particle movement due to the changes in microstructures, such as damage and breakage of hydrate crystals [17,19]. These interactions between the hydrate crystal and sediment particles as well as changes in the microstructure of sediments govern deformation behaviors and mechanical responses [40,41], as shown in Figure 9b.

At high hydrate saturation, the strength and stiffness of HBSs are enhanced evidently by the cementation of hydrate among sediment particles [42,43]. Several shear microplanes appear through hydrate mass if the bonding strength of the hydrate and particle is higher than hydrate strength [22]. Hydrate-particle cementation is destroyed along the hydrate-particle interface when the hydrate strength is higher, as shown in Figure 9b. Then, damage to hydrate crystal and the relative motion of mineral particles occur. Moreover, micro-fractures are formed with shear plane development.

The breakage of hydrate bonding and relative motion of mineral particles appear during the shearing process and then cause microstructural changes [44,45]. Uniform deformation and cracks are easily produced in samples, leading to destruction and failure [38,46], as illustrated in Figure 9a. During this process, strength and stiffness are enhanced obviously with the presence of hydrate.
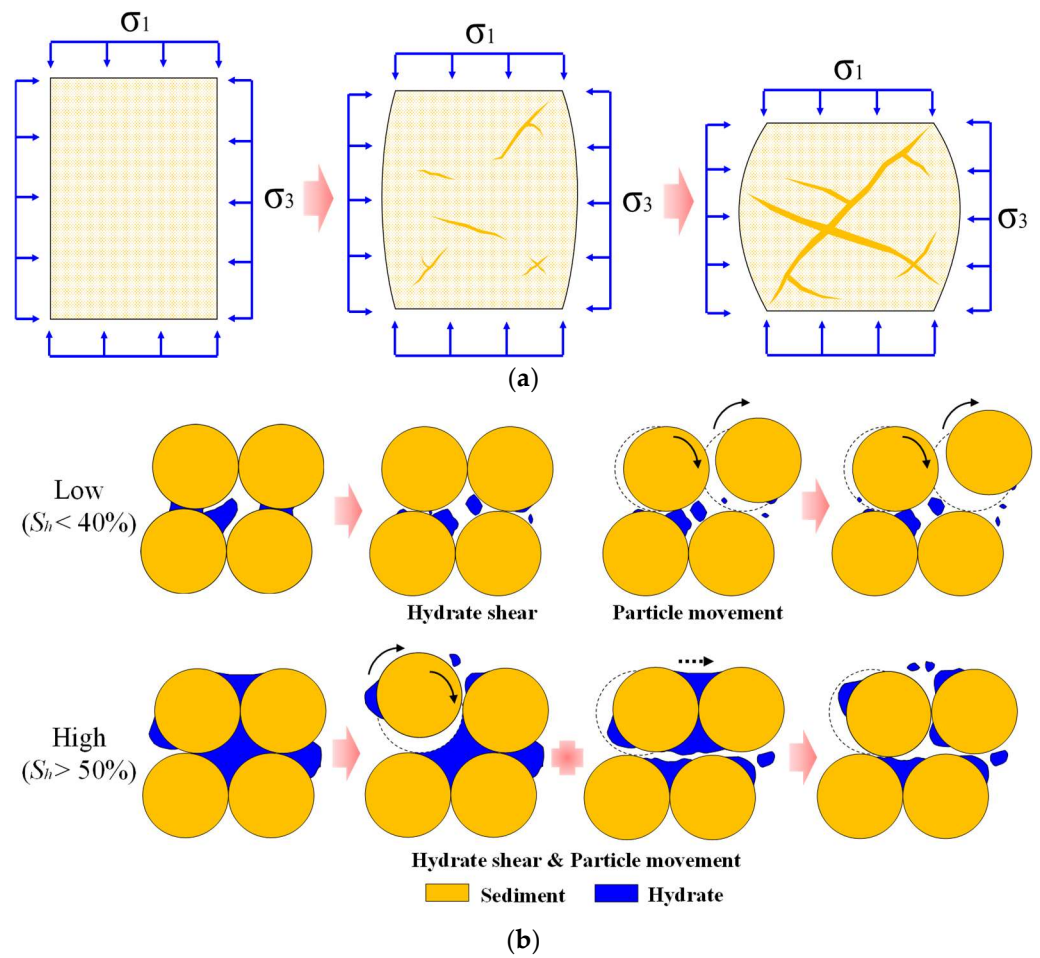
Figure 9. Failure mechanism of HBS: (**a**) Triaxial shearing process, (**b**) Failure mechanism during the shear process [40,41].

In addition, the fine particles and impurities, which exist in the pores of the clayey-silt samples, can restrict the formation of hydrate, and limit the movement of particles [15,33]. That makes the mechanical behaviors of reconstituted hydrate-bearing clayey-silt samples from the Shenhu area differ from that of sandy sediments containing hydrate.

4. Estimation of Strength Parameters

4.1. Failure Strength Prediction

As mentioned above, the failure strength of the sediments containing THF hydrate is mainly affected by effective confining pressure and hydrate saturation. Combining experimental results and the Drucker-Prager criterion [23,38], the improved model of failure strength can be expressed in Equations (3)–(5).

$$\sqrt{J_2} = K(S_h) + \beta(S_h) \cdot I_1 \tag{3}$$

$$J_2 = \frac{1}{6}\left[(\sigma_1 - \sigma_2)^2 + (\sigma_1 - \sigma_3)^2 + (\sigma_2 - \sigma_3)^2\right] \tag{4}$$

$$I_1 = \sigma_1 + \sigma_2 + \sigma_3 \tag{5}$$

where S_h represents hydrate saturation, %; K and β represent model coefficients related to hydrate saturation. Both K and β can be obtained via correlations of experimental data.

For the shearing tests, σ_2 and σ_3 are equal, Equation (3) can be expressed as:

$$\sigma_1 - \sigma_3 = \sqrt{3}K(S_h) + \sqrt{3}\beta(S_h) \cdot (\sigma_1 + 2\sigma_3) \tag{6}$$

$$\sigma_1 - \sigma_3 = \frac{\sqrt{3}K(S_h)}{1 - \sqrt{3}\beta(S_h)} + \frac{3\sqrt{3}\beta(S_h)}{1 - \sqrt{3}\beta(S_h)} \cdot \sigma_3 \tag{7}$$

Based on Equation (7), the failure strength $(\sigma_1 - \sigma_3)_s$ can be assumed as a function of hydrate saturation S_h and effective confining pressure σ_3 [23,38], which is given by Equations (8) and (9).

$$(\sigma_1 - \sigma_3)_f = A(S_h) + B(S_h) \cdot \sigma_3 \tag{8}$$

$$(\sigma_1 - \sigma_3)_f = 0.2303 \cdot S_h^{0.2298} \cdot \sigma_3 + 0.0564 \cdot S_h - 0.6075 \tag{9}$$

where $(\sigma_1 - \sigma_3)_f$ represents the failure strength of the HBS, MPa; *A* and *B* are model coefficients related to the hydrate saturation.

The prediction error is determined through Equations (10)–(12).

$$Error_{\min} = \min\left\{ \left| \frac{(\sigma_1 - \sigma_3)_{f\,pre} - (\sigma_1 - \sigma_3)_{f\,\exp}}{(\sigma_1 - \sigma_3)_{f\,\exp}} \right| \right\} \tag{10}$$

$$Error_{\max} = \max\left\{ \left| \frac{(\sigma_1 - \sigma_3)_{f\,pre} - (\sigma_1 - \sigma_3)_{f\,\exp}}{(\sigma_1 - \sigma_3)_{f\,\exp}} \right| \right\} \tag{11}$$

$$Error_{ave} = \frac{\sum\limits_{i=1}^{n} \left| \frac{(\sigma_1 - \sigma_3)_{f\,prei} - (\sigma_1 - \sigma_3)_{f\,\exp i}}{(\sigma_1 - \sigma_3)_{f\,\exp i}} \right|}{n} \tag{12}$$

where $Error_{\min}$, $Error_{\max}$, and $Error_{ave}$ are the minimum error, maximum error, and average error, respectively; $(\sigma_1 - \sigma_3)_{fpre}$ and $(\sigma_1 - \sigma_3)_{fexp}$ represent the prediction value and experimental value of the $(\sigma_1 - \sigma_3)_f$; $(\sigma_1 - \sigma_3)_{fprei}$ and $(\sigma_1 - \sigma_3)_{fexpi}$ are the ith prediction value and the ith experimental value of the $(\sigma_1 - \sigma_3)_f$.

Figure 10 demonstrates the comparison between the calculated strength and the experimental results of sediments with THF hydrate. It is observed that the improved Drucker-Prager criterion shows high fitting accuracy of failure strength. The shear stress of HBS under certain experimental conditions is matched by the improved criterion, with a maximum relative error of about 8.7% and an average relative error of about 3.3%, as shown in Figure 10b.
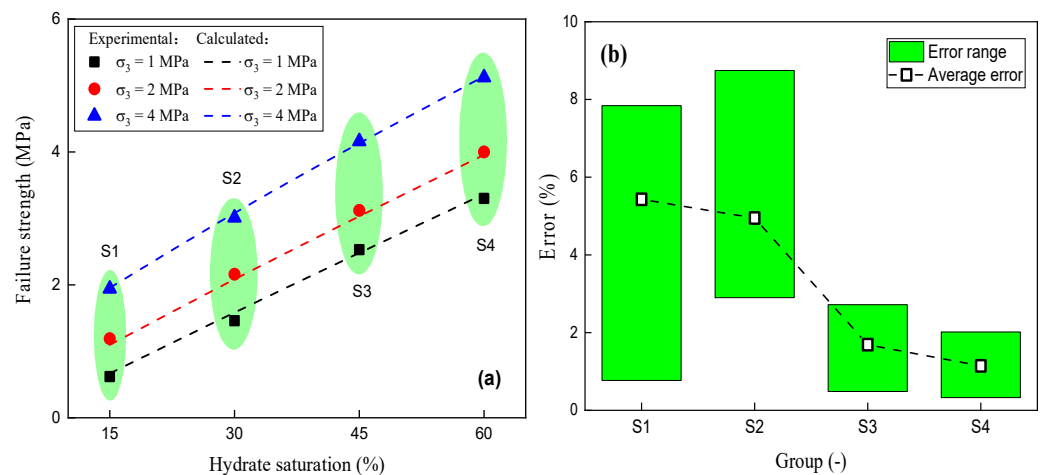

Figure 10. Comparison between experimental data and calculated results: (**a**) Predicted failure strength; (**b**) Error.

Figure 11 displays the prediction of failure strength. It can be observed that the failure strength of sediments containing THF hydrate can be approximately calculated by Equation (9) with knowing the stress state and hydrate saturation. Furthermore, improved strength calculating model and strength analysis could offer a precise prediction of mechan-

ical parameters for numerical simulations and key geological issues during gas hydrate exploitation of the South China Sea [7,8,10].
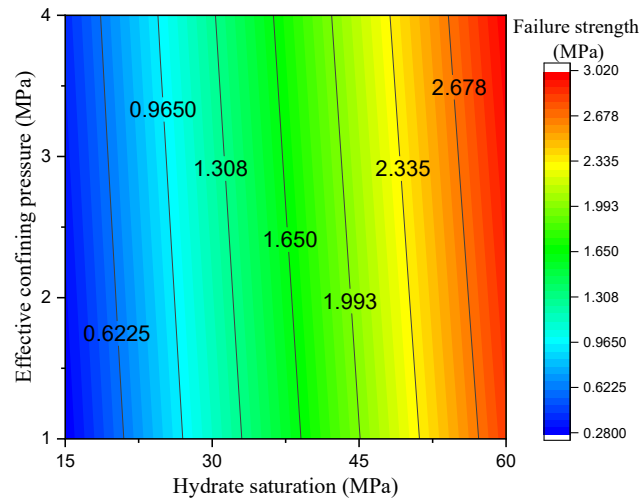

Figure 11. Calculation failure strength with this proposed model.

4.2. Young's Modulus Prediction

Young's modulus E_{50} mainly depends on the hydrate saturation and effective confining pressure [12,47]. Afterwards, Miyazaki et al. [48] established a model to predict the initial elastic modulus, as shown in Equation (13).

$$E_i = e_i(S_h) \cdot \sigma_3^n \tag{13}$$

where E_i represents the initial elastic modulus, MPa; σ_3 is the effective confining pressure, MPa; $e_i(S_h)$ represents the initial elastic modulus under σ_3 of 1 MPa, which is a function of hydrate saturation.

Similarly, Young's modulus E_{50} also can be estimated by proposing a calculation model. However, the assumed $e_i(S_h)$ limits the applicability and accuracy. Thus, we define this variable in the formula related to both hydrate saturation and effective confining pressure, which is given as:

$$E_{50} = f(\sigma_3) \cdot S_h + g(\sigma_3) \tag{14}$$

where f and g represent the functions of the effective confining pressure.

Based on the experimental data, the empirical equation can be defined as follows:

$$E_{50} = (0.0727 \cdot \sigma_3 + 1.2707) \cdot S_h + 2.053 \cdot \sigma_3^{2.3494} \tag{15}$$

Figure 12 exhibits the prediction of Young's modulus E_{50}. The average error is 8.0%. A comparison between calculated and experimental results shows that the calculation model has very good applicability and high forecast accuracy, as shown in Figure 12a. Furthermore, this model can be used to predict Young's modulus by considering hydrate saturation and stress state [19,38], as displayed in Figure 12b.

To summarize, both failure strength and Young's modulus can be decided quickly based on empirical equations obtained from experimental data. However, the precision and practicability of prediction are limited due to a lack of field data. Thus, more high reliability and accuracy tests are necessary both in the laboratory and field.
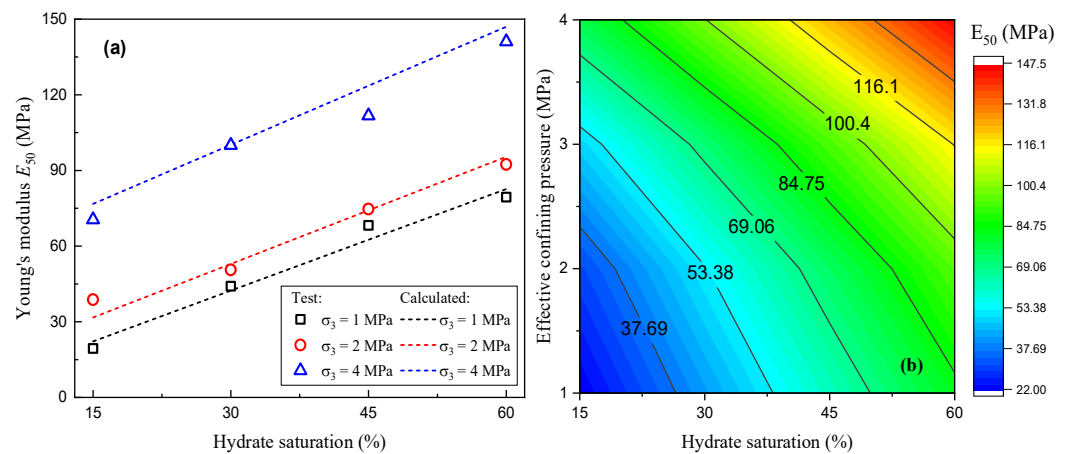
Figure 12. Prediction of Young's modulus: (**a**) Comparison between calculated and test results; (**b**) Prediction of Young's modulus based on the proposed empirical equation.

5. Conclusions

The stress-strain curves of the THF hydrate-bearing clayey-silt sediments showed obvious strain-hardening characteristics. The deviator stress increases rapidly at the small axial strain level (<3%) and then grows slowly with the increase in strain, which is obviously different from that of hydrate-bearing sand.

The failure strength and Young's modulus of reconstituted THF hydrate-bearing clayey-silt samples from the Shenhu area have a similar variation tendency to that of hydrate-bearing silty sediments. However, the differences in the value of strength parameters can be observed, which reflects the effect of sediment types, particle size distribution, hydrate types, and so on.

Macro-failure behaviors of reconstituted clayey-silt samples containing hydrate reveal the microstructure variations and microscopic interactions between hydrate crystal and mineral particles. Meanwhile, failure mechanisms of clayey-silt sediments containing hydrate are mainly determined by the collective effect of hydrate formation and the microstructure of sediments.

Failure strength is predicted by improved Drucker-Prager criterion with knowing hydrate characteristics and stress state. Moreover, the proposed calculation model based on experimental data can be used for predicting Young's modulus of hydrate-bearing clayey-silt sediments from the Shenhu area. It should be noted that high-reliability laboratory tests and empirical models are required for the numerical simulation and field operation due to lacking in-site data during the development of natural gas hydrate resources in the South China Sea.

References

1. Chong, Z.R.; Yang, S.H.B.; Babu, P.; Linga, P.; Li, X. Review of natural gas hydrates as an energy resource: Prospects and challenges. *Appl. Energy* **2016**, *162*, 1633–1652. [CrossRef]
2. Malagar, B.R.C.; Lijith, K.P.; Singh, D.N. Formation & dissociation of methane gas hydrates in sediments: A critical review. *J. Nat. Gas Sci. Eng.* **2019**, *65*, 168–184.
3. Li, X.; Xu, C.; Zhang, Y.; Ruan, X.; Li, G.; Wang, Y. Investigation into gas production from natural gas hydrate: A review. *Appl. Energy* **2016**, *172*, 286–322. [CrossRef]
4. Sánchez, M.; Gai, X.; Santamarina, J.C. A constitutive mechanical model for gas hydrate bearing sediments incorporating inelastic mechanisms. *Comput. Geotech.* **2017**, *84*, 28–46. [CrossRef]
5. Jiang, M.; Shen, Z.; Wu, D. CFD-DEM simulation of submarine landslide triggered by seismic loading in methane hydrate rich zone. *Landslides* **2018**, *15*, 2227–2241. [CrossRef]
6. Li, Y.; Ning, F.; Wu, N.; Chen, Q.; Nouri, A.; Hu, G.; Sun, J.; Kuang, Z.; Meng, Q. Protocol for sand control screen design of production wells for clayey silt hydrate reservoirs: A case study. *Energy Sci. Eng.* **2020**, *8*, 1438–1449. [CrossRef]
7. Wu, N.; Li, Y.; Chen, Q.; Liu, C.; Jin, Y.; Tan, M.; Dong, L.; Hu, G. Sand Production Management during Marine Natural Gas Hydrate Exploitation: Review and an Innovative Solution. *Energy Fuels* **2021**, *35*, 4617–4632. [CrossRef]
8. Wan, Y.; Wu, N.; Hu, G.; Xin, X.; Jin, G.; Liu, C.; Chen, Q. Reservoir stability in the process of natural gas hydrate production by depressurization in the shenhu area of the south China sea. *Nat. Gas Ind. B* **2018**, *5*, 631–643. [CrossRef]
9. Dong, L.; Wan, Y.; Li, Y.; Liao, H.; Liu, C.; Wu, N.; Leonenko, Y. 3D numerical simulation on drilling fluid invasion into natural gas hydrate reservoirs. *Energy* **2022**, *241*, 122932. [CrossRef]
10. Wei, J.; Yang, L.; Liang, Q.; Liang, J.; Lu, J.; Zhang, W.; Zhang, X.; Lu, X. Geomechanical properties of gas hydrate-bearing sediments in Shenhu Area of the South China Sea. *Energy Rep.* **2021**, *7*, 8013–8020. [CrossRef]
11. Wu, P.; Li, Y.; Sun, X.; Liu, W.; Song, Y. Mechanical Characteristics of Hydrate-Bearing Sediment: A Review. *Energy Fuels* **2021**, *35*, 1041–1057. [CrossRef]
12. Miyazaki, K.; Masui, A.; Sakamoto, Y.; Aoki, K.; Tenma, N.; Yamaguchi, T. Triaxial compressive properties of artificial methane-hydrate-bearing sediment. *J. Geophys. Res.* **2011**, *116*, B6. [CrossRef]
13. Song, Y.; Zhu, Y.; Liu, W.; Li, Y.; Lu, Y.; Shen, Z. The effects of methane hydrate dissociation at different temperatures on the stability of porous sediments. *J. Pet. Sci. Eng.* **2016**, *147*, 77–86. [CrossRef]
14. Dong, L.; Li, Y.; Liu, C.; Liao, H.; Chen, G.; Chen, Q.; Liu, L.; Hu, G. Mechanical Properties of Methane Hydrate-Bearing Interlayered Sediments. *J. Ocean. Univ. China* **2019**, *18*, 1344–1350. [CrossRef]
15. Hyodo, M.; Wu, Y.; Nakashima, K.; Kajiyama, S.; Nakata, Y. Influence of Fines Content on the Mechanical Behavior of Methane Hydrate-Bearing Sediments. *J. Geophys. Res. Solid Earth* **2017**, *122*, 7511–7524. [CrossRef]
16. Li, Y.; Dong, L.; Wu, N.; Nouri, A.; Liao, H.; Chen, Q.; Sun, J.; Liu, C. Influences of hydrate layered distribution patterns on triaxial shearing characteristics of hydrate-bearing sediments. *Eng. Geol.* **2021**, *294*, 106375. [CrossRef]
17. Lijith, K.P.; Malagar, B.R.C.; Singh, D.N. A comprehensive review on the geomechanical properties of gas hydrate bearing sediments. *Mar. Pet. Geol.* **2019**, *104*, 270–285. [CrossRef]
18. Li, Y.; Hu, G.; Wu, N.; Liu, C.; Chen, Q.; Li, C.A. Undrained shear strength evaluation for hydrate-bearing sediment overlying strata in the Shenhu area, northern South China Sea. *Acta Oceanol. Sin.* **2019**, *38*, 114–123. [CrossRef]
19. Liu, Z.; Wei, H.; Peng, L.; Wei, C.; Ning, F. An easy and efficient way to evaluate mechanical properties of gas hydrate-bearing sediments: The direct shear test. *J. Pet. Sci. Eng.* **2017**, *149*, 56–64. [CrossRef]
20. Dong, L.; Liao, H.; Li, Y.; Liu, C. Measurement and assessment of mechanical properties of hydrate-beraring sediments. *Mar. Geol. Front.* **2020**, *36*, 34–43.
21. Liu, Z.; Dai, S.; Ning, F.; Peng, L.; Wei, H.; Wei, C. Strength Estimation for Hydrate-Bearing Sediments from Direct Shear Tests of Hydrate-Bearing Sand and Silt. *Geophys. Res. Lett.* **2018**, *45*, 715–723. [CrossRef]
22. Yun, T.S.; Santamarina, J.C.; Ruppel, C. Mechanical properties of sand, silt, and clay containing tetrahydrofuran hydrate. *J. Geophys. Res. Solid Earth* **2007**, *112*, B4. [CrossRef]
23. Zhang, X.H.; Lu, X.B.; Shi, Y.H.; Xia, Z. Study on the mechanical properties of hydrate-bearing silty clay. *Mar. Pet. Geol.* **2015**, *67*, 72–80. [CrossRef]
24. Santamarina, J.C.; Dai, S.; Terzariol, M.; Jang, J.; Waite, W.F.; Winters, W.J.; Nagao, J.; Yoneda, J.; Konno, Y.; Fujii, T.; et al. Hydro-bio-geomechanical properties of hydrate-bearing sediments from Nankai Trough. *Mar. Pet. Geol.* **2015**, *66*, 434–450. [CrossRef]
25. Yoneda, J.; Masui, A.; Konno, Y.; Jin, Y.; Kida, M.; Katagiri, J.; Nagao, J.; Tenma, N. Pressure-core-based reservoir characterization for geomechanics: Insights from gas hydrate drilling during 2012–2013 at the eastern Nankai Trough. *Mar. Pet. Geol.* **2017**, *86*, 16. [CrossRef]
26. Masui, A.; Miyazaki, K.; Haneda, H.; Ogata, Y.; Aoki, K. Mechanical Properties of Natural Gas Hydrate Bearing Sediments Retrieved from Eastern Nankai Trough. In Proceedings of the Offshore Technology Conference, Houston, TX, USA, 5–8 May 2008; p. 10.
27. Luo, T.; Song, Y.; Zhu, Y.; Liu, W.; Liu, Y.; Li, Y.; Wu, Z. Triaxial experiments on the mechanical properties of hydrate-bearing marine sediments of South China Sea. *Mar. Pet. Geol.* **2016**, *77*, 507–514. [CrossRef]

28. Luo, T.; Li, Y.; Madhusudhan, B.N.; Zhao, J.; Song, Y. Comparative analysis of the consolidation and shear behaviors of CH4 and CO2 hydrate-bearing silty sediments. *J. Nat. Gas Sci. Eng.* **2020**, *75*, 103157. [CrossRef]

29. Li, Y.; Liu, L.; Jin, Y.; Wu, N. Characterization and development of marine natural gas hydrate reservoirs in clayey-silt sediments: A review and discussion. *Adv. Geo-Energy Res.* **2021**, *5*, 75–86. [CrossRef]

30. Li, Y.; Liu, C.; Liao, H.; Lin, D.; Bu, Q.; Liu, Z. Mechanical properties of the clayey-silty sediment-natural gas hydrate mixed system. *Nat. Gas Ind. B* **2021**, *8*, 154–162. [CrossRef]

31. Li, Y.; Liu, C.; Liu, L.; Sun, J.; Liu, H.; Meng, Q. Experimental study on evolution behaviors of triaxial-shearing parameters for hydrate-bearing intermediate fine sediment. *Adv. Geo-Energy Res.* **2018**, *2*, 43–52. [CrossRef]

32. Hyodo, M.; Li, Y.; Yoneda, J.; Nakata, Y.; Yoshimoto, N.; Nishimura, A.; Song, Y. Mechanical behavior of gas-saturated methane hydrate-bearing sediments. *J. Geophys. Res. Solid Earth* **2013**, *118*, 5185–5194. [CrossRef]

33. Kajiyama, S.; Hyodo, M.; Nakata, Y.; Yoshimoto, N.; Wu, Y.; Kato, A. Shear behaviour of methane hydrate bearing sand with various particle characteristics and fines. *Soils Found.* **2017**, *57*, 176–193. [CrossRef]

34. Liu, C.; Meng, Q.; He, X.; Li, C.; Ye, Y.; Zhang, G.; Liang, J. Characterization of natural gas hydrate recovered from Pearl River Mouth basin in South China Sea. *Mar. Pet. Geol.* **2015**, *61*, 14–21. [CrossRef]

35. Wei, J.; Liang, J.; Lu, J.; Zhang, W.; He, Y. Characteristics and dynamics of gas hydrate systems in the northwestern South China Sea–Results of the fifth gas hydrate drilling expedition. *Mar. Pet. Geol.* **2019**, *110*, 287–298. [CrossRef]

36. Li, Y.; Liu, C.; Liao, H.; Dong, L.; Bu, Q.; Liu, Z. Mechanical properties of the mixed system of clayey-silt sediments and natural gas hydrates. *Nat. Gas Ind.* **2020**, *40*, 159–168.

37. Jin, Y.; Li, Y.; Wu, N.; Yang, D. Characterization of Sand Production for Clayey-Silt Sediments Conditioned to Openhole Gravel-Packing: Experimental Observations. *SPE J.* **2021**, *26*, 3591. [CrossRef]

38. Dong, L.; Li, Y.; Liao, H.; Liu, C.; Chen, Q.; Hu, G.; Liu, L.; Meng, Q. Strength estimation for hydrate-bearing sediments based on triaxial shearing tests. *J. Pet. Sci. Eng.* **2020**, *184*, 106478. [CrossRef]

39. Madhusudhan, B.N.; Clayton, C.R.I.; Priest, J.A. The Effects of Hydrate on the Strength and Stiffness of Some Sands. *J. Geophys. Res. Solid Earth* **2019**, *124*, 65–75. [CrossRef]

40. Lei, L.; Santamarina, J.C. Physical properties of fine-grained sediments with segregated hydrate lenses. *Mar. Pet. Geol.* **2019**, *109*, 899–911. [CrossRef]

41. Waite, W.F.; Santamarina, J.C.; Cortes, D.D.; Dugan, B.; Espinoza, D.N.; Germaine, J.; Germaine, J.; Jang, J.; Jung, J.W.; Kneafsey, T.J.; et al. Physical properties of hydrate-bearing sediments. *Rev. Geophys.* **2009**, *47*, RG4003. [CrossRef]

42. Yan, C.; Ren, X.; Cheng, Y.; Song, B.; Li, Y.; Tian, W. Geomechanical issues in the exploitation of natural gas hydrate. *Gondwana Res.* **2020**, *81*, 403–422. [CrossRef]

43. Li, Y.; Wu, P.; Sun, X.; Liu, W.; Song, Y. Mechanical behaviors of hydrate-bearing sediment with different cementation spatial distributions at microscales. *iScience* **2021**, *24*, 102448. [CrossRef] [PubMed]

44. Yoneda, J.; Jin, Y.; Katagiri, J.; Tenma, N. Strengthening mechanism of cemented hydrate-bearing sand at microscales. *Geophys. Res. Lett.* **2016**, *43*, 7442–7450. [CrossRef]

45. Lei, L.; Gai, X.; Seol, Y. Load-bearing characteristic of methane hydrate within coarse-grained sediments–Insights from isotropic consolidation. *Mar. Pet. Geol.* **2020**, *121*, 104571. [CrossRef]

46. Kato, A.; Nakata, Y.; Hyodo, M.; Yoshimoto, N. Macro and micro behaviour of methane hydrate-bearing sand subjected to plane strain compression. *Soils Found.* **2016**, *56*, 835–847. [CrossRef]

47. Yan, C.; Cheng, Y.; Li, M.; Han, Z.; Zhang, H.; Li, Q.; Teng, F.; Ding, J. Mechanical experiments and constitutive model of natural gas hydrate reservoirs. *Int. J. Hydrogen Energy* **2017**, *42*, 19810–19818. [CrossRef]

48. Miyazaki, K.; Tenma, N.; Aoki, K.; Yamaguchi, T. A Nonlinear Elastic Model for Triaxial Compressive Properties of Artificial Methane-Hydrate-Bearing Sediment Samples. *Energies* **2012**, *10*, 4057–4075. [CrossRef]